Robust 3-D Path Following Control Framework for Magnetic Helical Millirobots Subject to Fluid Flow and Input Saturation

Zhaoyang Qi, *Student Member, IEEE*, Mingxue Cai, *Member, IEEE*, Bo Hao, Yanfei Cao, Lin Su, Xurui Liu, Kai Fung Chan, Chenguang Yang, *Fellow, IEEE*, and Li Zhang, *Fellow, IEEE*

Abstract—Precise trajectory control is imperative to ensure the safety and efficacy of *in vivo* therapy employing the magnetic helical millirobots. However, achieving accurate 3-D path following of helical millirobots under fluid flow conditions remains challenging due to the presence of the lumped disturbances, encompassing complex fluid dynamics and input frequency saturation. This study proposes a robust 3-D path following control framework that combines a disturbance observer for perturbation estimation with an adaptive finite-time sliding mode controller for autonomous navigation along the reference trajectories. First, a magnetic helical millirobot's kinematic model based on the 3-D hand position approach is established. Subsequently, a robust smooth differentiator is implemented as an observer to estimate disturbances within a finite time. We then investigate an adaptive finite-time sliding mode controller incorporating an auxiliary system to mitigate the estimated disturbance and achieve precise 3-D path tracking while respecting the input constraints. The adaptive mechanism of this controller ensures fast convergence of the system while alleviating the chattering effects. Finally, we provide a rigorous theoretical analysis of the finite-time stability of the closed-loop system based on the Lyapunov functions. Utilizing a robotically-actuated magnetic manipulation system, experimental results demonstrate the efficacy of the proposed approach in terms of the control accuracy and convergence time.

Index Terms—3-D path tracking, flow rates, helical millirobots, magnetic actuation.

Zhaoyang Qi, Bo Hao, Yanfei Cao, Lin Su, and Xurui Liu are with the Department of Mechanical and Automation Engineering, The Chinese University of Hong Kong (CUHK), Hong Kong, China.

Mingxue Cai is with the Shenzhen Institute of Advanced Technology (SIAT), Guangdong Provincial Key Laboratory of Robotics and Intelligent System, Chinese Academy of Sciences, Shenzhen 518055, China.

Kai Fung Chan is with the Chow Yuk Ho Technology Centre for Innovative Medicine, Li Ka Shing Institute of Health Sciences, The Chinese University of Hong Kong, Hong Kong, China.

Chenguang Yang is with the Department of Computer Science, University of Liverpool, L69 3BX Liverpool, U.K. (e-mail: cyang@ieee.org).

Li Zhang is with the Department of Mechanical and Automation Engineering, Chow Yuk Ho Technology Centre for Innovative Medicine, CUHK T Stone Robotics Institute, The Chinese University of Hong Kong, Hong Kong, China (e-mail: lizhang@mae.cuhk.edu.hk).

I. INTRODUCTION

IN THE past few decades, helical millirobots driven by external magnetic fields have been intensively investigated owing to their potential for the cell transport, precise drug delivery, and minimally invasive therapy [1], [2], [3], [4], [5], [6], [7], [8], [9], [10]. The propulsion mechanism of magnetic helical millirobots, specifically the transduction of magnetic torque for locomotion and orientation control, has been studied in the previous literature [11], [12], [13]. To fully exploit the potential of the helical millirobots in various applications, developing a path following controller for a helical millirobot to achieve satisfactory performance has become a critical issue [14], [15], [16], [17], [18]. However, addressing this issue presents challenges stemming from intricate biofluidic dynamics, luminal boundary effects, and input frequency saturation.

As helical millirobots behave as nonholonomic systems, several control laws for the nonholonomic autonomous robots have been investigated and applied to the path following control of the helical millirobots. Samson developed a planar path following controller for a wheeled robot by linearizing a kinematic model using a chained form and then applying a linear control law [19]. Inspired by the chained form the approach, Xu et al. [13] converted the kinematic model of a helical millirobot into a linear model using the chained form approach, realizing straight-line path following in the horizontal plane. To achieve the 3-D path tracking of helical millirobots in a closed loop, Oulmas et al. designed a novel chained formulation to linearize the kinematic model in higher dimensions. The fundamental concept in the aforementioned studies relies on transforming the dynamics of the helical millirobots into a chained form using the Serret–Frenet frame. Although the aforementioned control methodologies demonstrate efficacy in static environments, they do not adequately address the complex disturbances inherent in real-world scenarios.

Recent research have increasingly focused on developing the robust nonlinear control strategies to facilitate the translation of magnetic robots to diverse real-world applications.

Zhao et al. [20] proposed two closed-loop path following controllers based on steering and rotational frequency control for on-plane docking of magnetic helical microrobots, potentially enhancing the precision of microoperations.

To compensate for the gradient force applied to the helical millirobot while implementing the 3-D path following tasks, a direct model reference adaptive controller (MRAC) was implemented to perform inverse magnetics calculations and gradient force compensation [21]. In [22], a PID regulator was incorporated into the visual serving control to keep the helical millirobot on the desired trajectory during the blood clot removal. Considering the disturbances caused by boundary effects and the weight of the helical millirobot, an orientation-compensation model of the helical millirobot's dynamics in the global coordinate frame was learned by appropriate backpropagation algorithms [23]. In addition, a proxy-based sliding-mode control (PSMC) approach was devised based on a kinematic error model to drive the helical millirobot toward the reference path effectively. However, the fixed values of PID control parameters in PSMC limited its robustness performance. Yang et al. [24] developed an SMC controller to realize the large-workspace navigation control of a rolling microrobot. To address the lumped disturbances of the system, a conservative operation was employed to introduce a large gain into the designed SMC controller, which resulted in the chattering problem. Furthermore, another limitation of the aforementioned SMC controllers is the lack of guarantee for finite-time stability during path following. It is widely acknowledged that achieving the finite-time stabilization of the dynamical systems can lead to fast convergence to the equilibrium point and superior disturbance attenuation simultaneously [25].

In summary, the aforementioned research works have provided valuable insight into applying the chained form the approach or nonlinear control laws for the helical millirobots. However, many of these studies did not consider the complex fluid environment, which is a crucial factor when deploying the helical millirobots in biofluid environments [26]. Among these, the sliding mode control algorithm has been proposed as a robust approach for handling the model uncertainties and driving the sliding variables to zero. Moreover, it has been validated that the SMC control laws with corresponding disturbance observers can achieve improved path following performance [27], [28], [29]. In addition to fluid flow, another control challenge for the helical millirobots arises from the upper limit on the rotational frequency around their principal axis. This limit, known as the step-out characteristic frequency, represents the maximum rotational frequency at which the robot remains synchronized with the external rotating field [7]. Beyond this threshold, the velocity of the helical millirobots rapidly decreases. To navigate in three dimensions within fluid flow environments, the rotational frequency of the helical millirobot must be increased to overcome the external fluid flow. Therefore, considering the step-out frequency as input saturation is essential for effective control. In a study by Mohammadi and Spong [30], an integral line of sight (ILOS) path following control method based on an optimal decision strategy (ODS) was proposed to make a helical millirobot
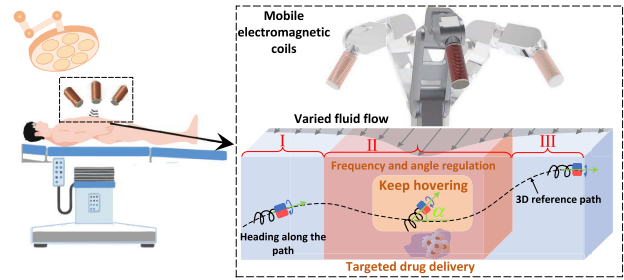

Fig. 1. Schematic of the 3-D automatic navigation and targeted hovering of a magnetic helical millirobot within a dynamic biofluid environment. The mobile electromagnetic coils can generate a desired rotating magnetic field, enabling the actuation of the millirobot in a human-sized workspace. In phases I and III, where the influence of fluid flow is weak, the millirobot follows a preprogrammed path under the guidance of the rotating field. In phase II, when fluid flow becomes more significant, the millirobot automatically adjusts its rotation frequency and heading to resist the varying fluid flow, allowing it to accurately track the desired path or maintain a stable hovering position for targeted drug delivery.

converge to a straight line while respecting the step-out frequency. However, the main limitation of this method is the possibility of integrator wind-up, which is inherent to the ILOS-based family of controllers.

In this study, considering the potential application of the helical millirobots in biomedical scenarios subject to the lumped disturbances (Fig. 1), a robust 3-D path following control framework is proposed for navigation and validated through the robotically-actuated magnetic manipulation system. This lumped disturbance covers intricate biofluidic dynamics, input saturation, luminal boundary effects, and gravity force. First, we formulate a kinematics model of the helical millirobot using a 3-D hand position approach. Subsequently, we propose an adaptive finite-time sliding mode control (AFTSMC) approach integrated with a finite-time disturbance observer (FTDOB) to achieve finite-time convergence under the lumped disturbances. Finally, the performance of the proposed control framework is validated through the extensive experiments. The main contributions of this study are summarized as follows.

1) Aiming at the nonholonomic and underactuated properties of the helical millirobot under the lumped disturbances, we formulate a magnetically actuated kinematic model of the helical millirobot using a 3-D hand position approach.

2) A robust control law, comprising of the AFTSMC algorithm with the FTDOB, is presented to ensure the practical convergence of the helical millirobot to a reference path. An adaptive mechanism has been designed based on the disturbances estimated by the FTDOB to ensure the convergence of the control variables within a reasonable time and mitigate the chattering phenomena. Furthermore, an auxiliary dynamics system is introduced to solve the input saturation. The stability analysis of the proposed controller is conducted using a Lyapunov function, demonstrating the finite-time convergence of the sliding variables.

3) Utilizing a robotically-actuated magnetic manipulation system, experimental applications to a helical millirobot

prototype validates the efficacy of the proposed control framework in terms of precision and convergence time in complex fluids.

The remainder of this article is organized as follows. Section II presents the magnetic manipulation and kinematic modeling of a helical millirobot. In Section III, we formulate the 3-D path following control for a helical millirobot subjected to the lumped disturbances, along with the corresponding stability analysis. Thereafter, the experimental results are presented and discussed in Section IV. Finally, Section V concludes this article.

Notation: Throughout this article, we use standard lowercase to represent the scalars (e.g., v) and bold lowercase for the column vectors (e.g., $\mathbf{v} = [v_x, v_y, v_z]^T$). The Euclidean norm of a vector is expressed as $\|\mathbf{v}\|$. The hat notation denotes an unit vector or normalized direction of a vector (e.g., $\hat{\mathbf{v}} = \mathbf{v}/\|\mathbf{v}\|$). The uppercase blackboard symbol $\mathbb{M}$ indicates the matrix, and the symbol $\mathcal{R}$ represents the set of all the non-negative real numbers. Given a vector $\boldsymbol{x} \in \mathcal{R}^n$ and scalar $\rho > 0$, $\text{sig}^\rho(\boldsymbol{x}) = |\boldsymbol{x}|^\rho \text{sign}(\boldsymbol{x})$. Let $^w\mathbf{v}$ indicates the coordinates of the vector $\mathbf{v} \in \mathcal{R}^n$ in the coordinate frame w. Moreover, the power of vectors is defined as: $\boldsymbol{z}^{[\rho]} = (z_1^{[\rho]}, z_2^{[\rho]}, \ldots, z_n^{[\rho]})$.

II. PROBLEM FORMULATION AND PRELIMINARY

In this section, we first introduce the magnetic manipulation of a helical millirobot. Then, the kinematic model of the helical millirobot is constructed based on the 3-D hand position approach.

A. Magnetic Manipulation Method

When the helical millirobot comprising magnetic materials is wirelessly actuated under an externally imposed magnetic field $\mathbf{b} \in \mathcal{R}^3$, the magnetic torque $\mathbf{T}_m \in \mathcal{R}^3$, and the magnetic force $\mathbf{F}_m \in \mathcal{R}^3$ are generated and given as follows:

$$\begin{cases} \mathbf{T}_m = \int_{V_m} (\mathbf{m} \times \mathbf{b}) dV_m \\ \mathbf{F}_m = \int_{V_m} \nabla(\mathbf{m} \cdot \mathbf{b}) dV_m \end{cases} \tag{1}$$

where $\mathbf{m} \in \mathcal{R}^3$ is the magnetization of the object, and the integration is performed over the magnetized object's volume V_m.

In this study, the helical millirobot is actuated using a magnetic actuation system equipped with three mobile electromagnetic coils. By superimposing three linearly independent magnetic field vectors $\hat{\mathbf{b}}_e$, generated by passing current through coils $\mathbf{i} = [i_1, i_2, i_n]^T$, any desired magnetic field vector in position $^w\mathbf{p} \in \mathcal{R}^3$ can be obtained

$$\mathbf{b}(^w\mathbf{p}) = \sum_{e=1}^{3} \hat{\mathbf{b}}_e(^w\mathbf{p}) i_e. \tag{2}$$

Under the magnetic field $\mathbf{b}(^w\mathbf{p})$, an unconstrained helical millirobot will experience the magnetic torque $\mathbf{T}_m$ derived in (1) and always attempt to align its dipole moment with the applied field for the quasi-static manipulations. Subsequently, when subjected to a rotating field with the rotational frequency $\mathbf{w}_\mathcal{H} \in \mathcal{R}^3$ in a local region, the helical millirobot tends to keep in synchrony with the external rotating field, inducing the

forward motion and orientation regulation. According to [31], the forward velocity $\mathbf{v}_\mathcal{H} \in \mathcal{R}^3$ of the helical millirobot can be implemented by the rotational frequency $\mathbf{w}_\mathcal{H}$ as follows:

$$\mathbf{v}_\mathcal{H} = \mathbb{C}\mathbf{w}_\mathcal{H} \tag{3}$$

where $\mathbb{C} \in \mathcal{R}^{3\times3}$ depends on the geometry of the helical millirobot and fluid environment properties. As $\mathbb{C}$ is invertible, the rotational frequency $\mathbf{w}_\mathcal{H}$ can be expressed as follows:

$$\mathbf{w}_\mathcal{H} = \mathbb{C}^{-1}\mathbf{v}_\mathcal{H}. \tag{4}$$

In addition, the magnetic actuation system can adjust the position of the electromagnetic coils to keep pace with the helical millirobot, ensuring that the coils and the millirobot maintain a fixed relative position. Therefore, the required forward velocity $\mathbf{v}_\mathcal{H}$ can be determined by regulating the rotational frequency $\mathbf{w}_\mathcal{H}$ while the desired forward direction can be generated by regulating the rotational axis, thereby controlling the helical millirobot to track a 3-D reference path.

Remark 1: The apparent weight of millirobots, which is defined as the difference between the gravity and the buoyancy force, is nonzero, thus causing the millirobots drift downward. Moreover, several factors, such as the biofluidic dynamics and luminal boundary effects, are all considered as disturbances that must be corrected in the kinematic model. Therefore, the 3-D path following of a helical millirobot requires a robust control law to compensate for the lumped disturbances. Besides, when a rotating field is applied to the helical millirobot, its forward velocity grows linearly along with the increase of the rotation field frequency, but will rapidly decline once the "step-out" characteristic frequency is reached [7]. In this article, the saturation constraint of the rotating field frequency is also considered for the controller design.

B. System Model

The kinematic equation of the helical millirobot in the 3-D space is given by the following five-DOF mathematical model as follows:

$$\begin{cases} \dot{x} = u\cos(\psi)\cos(\theta) - v\sin(\psi) + w\cos(\psi)\sin(\theta) \\ \dot{y} = u\sin(\psi)\cos(\theta) + v\cos(\psi) + w\sin(\psi)\sin(\theta) \\ \dot{z} = -u\sin(\theta) + w\cos(\theta) \\ \dot{\theta} = q \\ \dot{\psi} = r/\cos(\theta) \end{cases} \tag{5}$$

where $[x, y, z]$ represents the position. θ and ψ are the pitch and yaw angles (all in the world frame $\mathcal{W}$), which can be expressed by the tracking output $\boldsymbol{\eta} = [x, y, z, \theta, \psi]^T$; while $[u, v, w]$ represents the linear velocity. q and r are the angular velocities in the pitch and yaw directions (all in the body frame $\mathcal{H}$).

Considering the underactuated property for this control issue, the kinematic model (5) of the helical millirobot can be decomposed into actuated and unactuated dynamics as follows:

$$\dot{\boldsymbol{\eta}} = \mathbb{R}(\boldsymbol{\eta})\boldsymbol{u}_a + \boldsymbol{\delta}(\boldsymbol{\eta}, \boldsymbol{w}) \tag{6}$$

where $\boldsymbol{u}_a = [u, q, r]^T$ and $\boldsymbol{w} = [v, w]^T$ denote the velocity vectors of the helical millirobot in the actuated and unactuated directions, respectively. $\mathbb{R}(\boldsymbol{\eta})$ and $\boldsymbol{\delta}(\boldsymbol{\eta}, \boldsymbol{w})$ can be considered
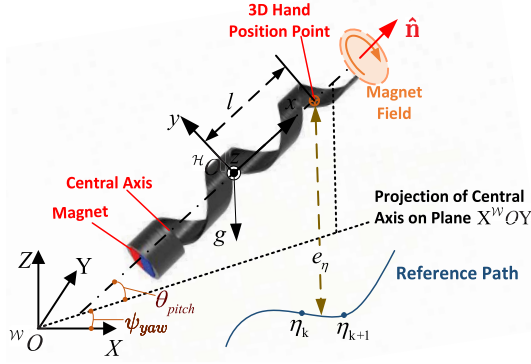
Fig. 2. Definitions of world frame $\mathcal{W}$ and body frame $\mathcal{H}$. The helical millirobot is actuated by rotating magnetic fields to follow a reference path using a selected 3-D hand position point.

as the kinematic matrix and the kinematic disturbance, which can be expressed as

$$
\mathbb{R}(\boldsymbol{\eta}) = \begin{bmatrix} \cos(\psi)\cos(\theta) & 0 & 0 \\ \sin(\psi)\cos(\theta) & 0 & 0 \\ -\sin(\theta) & 0 & 0 \\ 0 & 1 & 0 \\ 0 & 0 & \frac{1}{\cos(\theta)} \end{bmatrix}
$$

$$
\boldsymbol{\delta}(\boldsymbol{\eta}, \boldsymbol{w}) = \begin{bmatrix} -v\sin(\psi) + w\sin(\theta)\cos(\psi) \\ v\cos(\psi) + w\sin(\theta)\sin(\psi) \\ w\cos(\theta) \\ 0 \\ 0 \end{bmatrix}. \quad (7)
$$

For the tracking output $\boldsymbol{\eta}$ of the control system in (6), one common selection is the geometric center of the controlled object. However, the main issue is that this geometric center coordinate is not affected by the control inputs in yaw and pitch directions. Especially for this control issue with an under-actuated property, the singularity in the kinematic matrix (7) introduces the unstable internal dynamics into the control system [32]. To address this problem, we drew inspiration from the literature [32], [33] to extend the definition of the hand position point to the 3-D hand position approach of the helical millirobots. Hence, the tracking output is set as the position of a virtual point placed on the longitudinal symmetry axis of the helical millirobot, at a positive constant l from the midpoint of the principal axis (see Fig. 2), which is now rewritten as follows:

$$
\boldsymbol{h}(\boldsymbol{\eta}) = \begin{bmatrix} x + l\cos(\theta)\cos(\psi) \\ y + l\cos(\theta)\sin(\psi) \\ z - l\sin(\theta) \end{bmatrix}. \quad (8)
$$

By differentiating (8), the kinematic model of the helical millirobot can be rearranged into 3-D hand position dynamics as follows:

$$
\dot{\boldsymbol{h}}(\boldsymbol{\eta}) = \mathbb{J}(\boldsymbol{\eta})\boldsymbol{u}_a + \boldsymbol{J}_\delta(\boldsymbol{\eta}, \boldsymbol{w}) \quad (9)
$$

where $\boldsymbol{u}_a = [u, q, r]^T$ denotes the velocity vector of a helical millirobot in the actuated direction in the frame $\mathcal{H}$. $\mathbb{J}(\boldsymbol{\eta})$ is regarded as the transformation matrix denoting the effect of internal dynamics, and $\boldsymbol{J}_\delta(\boldsymbol{\eta}, \boldsymbol{w})$ can be regarded as the

input-output map of the kinematic lumped disturbances in the world frame $\mathcal{W}$, including external disturbance and system uncertainties, which can be expressed by

$$
\mathbb{J}(\boldsymbol{\eta}) = \begin{bmatrix} \cos(\psi)\cos(\theta) & -l\sin(\theta)\cos(\psi) & -l\sin(\psi) \\ \sin(\psi)\cos(\theta) & -l\sin(\theta)\sin(\psi) & l\cos(\psi) \\ -\sin(\theta) & -l\cos(\theta) & 0 \end{bmatrix}
$$

$$
\boldsymbol{J}_\delta(\boldsymbol{\eta}, \boldsymbol{w}) = \begin{bmatrix} -v\sin(\psi) + w\sin(\theta)\cos(\psi) \\ v\cos(\psi) + w\sin(\theta)\sin(\psi) \\ w\cos(\theta) \end{bmatrix}.
$$

In (8), when $l > 0$, the yaw angle ψ, and pitch angle θ play a significant role in influencing the tracking output. Hence, the effective control for the orientation angle of the millirobot becomes crucial in maintaining the stability of the 3-D hand position point. In contrast to the kinematic matrix (7), no singularity exists in the matrix $\mathbb{J}(\boldsymbol{\eta})$ for all $\theta, \psi \in \mathcal{R}$.

III. CONTROL FRAMEWORK AND STABILITY ANALYSIS

The control objective of this article is to design appropriate guidance and control laws $\boldsymbol{u}_a$ which can drive the helical millirobot to follow a 3-D reference path $\boldsymbol{\ell}_\eta = [x_d, y_d, z_d]^T \in \mathcal{R}^3$, while all the signals in the closed-loop control system are guaranteed to be bounded, and tracking errors of the helical millirobot converge to an arbitrarily small vicinity of the sliding surface within the finite time. To this end, the design of the control framework is a two-step process. First, the FTDOB is implemented to provide the fast estimation of the time-varying lumped disturbance. In the second step, the AFTSMC approach and an auxiliary system are constructed to calculate the desired velocity and the angular rate $\boldsymbol{u}_a$, utilizing the estimation of the lumped disturbances in the first step. The control structure of the helical millirobot is shown in Fig. 3.

The following assumption and lemma will be utilized in the observer design.

Assumption 1 [34]: The lumped disturbance $\boldsymbol{J}_\delta$ and its derivative are assumed to be unpredictable, varying, and limited in energy, so the unknown disturbance and its derivative satisfy $\boldsymbol{J}_\delta \leq \alpha < \infty$ and $\dot{\boldsymbol{J}}_\delta \leq \beta < \infty$, where α and β are the bounded constants.

Lemma 1 [35]: For the differentiator taking on the form as

$$
\begin{cases} \dot{\xi}_0(t) = v_0(t) + u(t) \\ v_0(t) = -\lambda_0|\xi_0 - f_0(t)|^{\frac{n}{n+1}}\text{sign}(\xi_0 - f_0(t)) + \xi_1(t) \\ \dot{\xi}_1(t) = v_1(t) \\ v_1(t) = -\lambda_1|\xi_1 - v_0|^{\frac{n-1}{n}}\text{sign}(\xi_1 - v_0) + \xi_2(t) \\ \vdots \\ \dot{\xi}_{n-1}(t) = v_{n-1}(t) \\ v_{n-1}(t) = -\lambda_{n-1}|\xi_{n-1} - v_{n-2}|^{\frac{1}{2}}\text{sign}(\xi_{n-1} - v_{n-2}) + \xi_n(t) \\ \dot{\xi}_n(t) = -\lambda_n\text{sign}(\xi_n - v_{n-1}). \end{cases}
$$

The following equalities could hold in the absence of input noises after a finite time of transient process:

$$
\xi_0 = f_0(t); \; \xi_i = v_{i-1} = f_0^{(i)}(t), \; (i = 1, \dots, n).
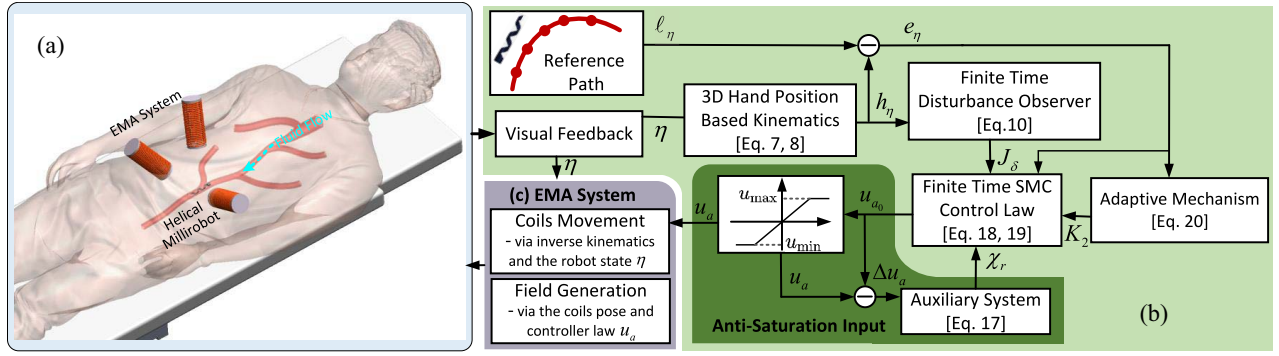$$

Fig. 3.   Structure of the proposed control framework of helical millirobot for 3-D path tracking. (a) Endoluminal procedures illustrate how the helical millirobot performs the path tracking under magnetic actuation *invivo*. (b) Proposed control framework comprises the adaptive finite-time SMC, FTDOB, and auxiliary system. (c) EMA can adjust the position of the electromagnetic coils to keep pace with the helical millirobot, while the generated magnetic field can drive the millirobot to the reference path.

A. Estimation of Lumped Disturbance

In this study, a finite-time observer to estimate the lumped disturbance can be designed as follows:

$$
\begin{cases}
\dot{\hat{h}}_\eta = V_\eta + \hat{J}_\delta \\
\dot{\hat{J}}_\delta = -\lambda_{\beta_1}\left|\hat{h}_\eta - h_\eta\right|^{1/2}\text{sign}\left(\hat{h}_\eta - h_\eta\right) + \hat{J}^* \\
\dot{\hat{J}}^* = -\lambda_{\beta_2}\text{sign}\left(\hat{J}^* - J_\delta\right)
\end{cases}
\tag{10}
$$

where $\dot{\hat{h}}_\eta$ and $\hat{J}_\delta$ represent the estimation of the motion velocity and the lumped disturbance in the frame $\mathcal{W}$. V_η denotes the transformed velocity vector in the frame $\mathcal{W}$, and J^* is an intermediate variable. The parameters λ_{β_1} and λ_{β_2} are the observer's positive gains, which determine the convergence rate. Taking the estimation errors as $\tilde{h}_\eta = \hat{h}_\eta - h_\eta$ and $\tilde{J}^* = \hat{J}^* - J_\delta$, differentiating $\tilde{h}_\eta$ and $\tilde{J}^*$ with respect to time, the estimation error equations can be written in the form of

$$
\begin{cases}
\dot{\tilde{h}}_\eta = -\lambda_{\beta_1}\tilde{h}_\eta^{1/2}\text{sign}\left(\tilde{h}_\eta\right) + \tilde{J}^* \\
\dot{\tilde{J}}^* = -\lambda_{\beta_2}\text{sign}\left(\hat{h} - J_\delta\right) - \dot{J}_\delta
\end{cases}
\tag{11}
$$

where $\dot{J}_\delta$ corresponds to the derivative of the disturbance that is assumed to be bounded for all $t \geq 0$ referring to Assumption 1. According to the Lemma 1, the state estimation of the lumped disturbance can be reached after a finite time

$$
\hat{J}^* = J_\delta
\tag{12}
$$

with the error dynamics converging to the bounded region. Following the similar manners as in [36], the finite time of the transient process T_1 is given by:

$$
T_1 \leq \frac{2}{\zeta}V_0^{1/2}
\tag{13}
$$

where V_0 is a positive definite quadratic function denoted by $V_0 = s^T\boldsymbol{\Gamma}s$ with the vector $s = [|\tilde{h}_\eta|^{(1/2)}\text{sign}(\tilde{h}_\eta), \text{sign}(\tilde{J}^*)]^T$. The parameter $\boldsymbol{\Gamma}$ is a constant, symmetric, and positive definite matrix, while ζ denotes the constant related to the reaching time.

The following assumption and lemma will be utilized in the controller design:

Assumption 2 [37]: In practice, as described about the frequency saturation in *Remark 1*, the control law (velocity vector) u_a determined by the saturated function of the nominal control command u_{a_0} can be described by

$$
u_a = \text{sat}(u_{a_0}) = \text{sign}(u_{a_0})\min\{|u_{a_0}|, u_{a,\max}\}
\tag{14}
$$

where $u_{a,\max}$ denotes the positive magnitude constraint.

Lemma 2 [38]: The nth-order smooth nonlinear switching function $F(X) : \mathcal{R} \to \mathcal{R}$ can be represented as

$$
F(X) = \begin{cases}
0, & \text{if } |X| \leq X_a \\
1 - \cos^n\left(\frac{\pi}{2}\sin^n\left(\pi\frac{|X|^2 - X_a^2}{2X_b^2 - 2X_a^2}\right)\right), & \text{otherwise} \\
1, & \text{if } |X| \geq X_b.
\end{cases}
$$

The condition is $0 < X_a < X_b$, where X_a and X_b are arbitrarily small positive design constants to determine the transient progress within (X_a, X_b) and the robust control region outside of (X_a, X_b).

B. Design of Adaptive Finite-Time Sliding Mode Control

This section aims to introduce the proposed AFTSMC control framework of the helical millirobot for the 3-D path tracking. To begin with, a sliding manifold needs to be designed such that the system trajectory along the manifold acquires specific desired properties, such as error convergence. Based on the helical model for the path tracking task, the integral sliding mode surface is defined as follows:

$$
\boldsymbol{S}_r = \boldsymbol{e}_\eta + \int_0^t \alpha_e\boldsymbol{e}_\eta(\tau) + \beta_e\boldsymbol{e}_\eta^{m/n}(\tau)\text{sign}(\boldsymbol{e}_\eta(\tau))d\tau
\tag{15}
$$

where $\boldsymbol{e}_\eta = \boldsymbol{h}_\eta - \boldsymbol{\ell}_\eta$ represents the tracking error between the actual state vectors $\boldsymbol{h}_\eta = [x, y, z]^T \in \mathcal{R}^3$ and the reference path $\boldsymbol{\ell}_\eta = [x_d, y_d, z_d]^T \in \mathcal{R}^3$. m and n are the odd integers satisfying $0 < m/n < 1$. α_e and β_e are strictly positive constants, which influence the convergence rate of the tracking error. With the 3-D hand position approach, the error dynamics of the closed-loop system can be derived by taking the time derivative of the sliding-mode surface $\boldsymbol{S}_r$ as

$$
\begin{aligned}
\dot{\boldsymbol{S}}_r &= \mathbb{J}(\boldsymbol{\eta})\boldsymbol{u}_a + \boldsymbol{J}_\delta(\boldsymbol{\eta}, \boldsymbol{w}) - \dot{\boldsymbol{\ell}}_\eta \\
&\quad + \alpha_e\boldsymbol{e}_\eta + \beta_e\boldsymbol{e}_\eta^{m/n}\text{sign}(\boldsymbol{e}_\eta).
\end{aligned}
\tag{16}
$$

In dynamic fluid environments, the millirobot needs to increase its rotational frequency to counteract the impact of the

flow rate. However, violating the upper limit on the rotation frequency will lead to step-out and undermine the control accuracy. So, it is preferable to eliminate the adverse effect induced by the frequency constraint. Hence, we propose to incorporate an auxiliary dynamic system that provides the feedback on the saturation values to a finite-time stability system [39]. The states of this auxiliary system are utilized to devise the adaptive control strategy designed as follows:

$$\dot{\boldsymbol{\chi}}_r = -k_1 \boldsymbol{\chi}_r - F(\boldsymbol{\chi}_r) \frac{\left| \boldsymbol{S}_r^T \Delta \boldsymbol{u}_a \right| + 0.5 \rho_r^2 \Delta \boldsymbol{u}_a^T \Delta \boldsymbol{u}_a}{\boldsymbol{\chi}_r}$$
$$- k_2 \mathrm{sig}^\rho(\boldsymbol{\chi}_r) + \rho_r \Delta \boldsymbol{u}_a \qquad (17)$$

where $\boldsymbol{\chi}_r \in \mathbb{R}^3$ is the auxiliary state variable. k_1, k_2, and ρ_r denote the positive gain constants. ρ can be any value within $(0, 1)$ and $F(\boldsymbol{\chi}_r)$ is defined as in Lemma 2. $\Delta \boldsymbol{u}_a = \boldsymbol{u}_a - \boldsymbol{u}_{a_0} = \mathrm{sat}(\boldsymbol{u}_{a_0}) - \boldsymbol{u}_{a_0}$ is the input saturation value, representing the difference associated with practical perspective and nominal control command. In the light of the helical millirobot dynamics in the presence of the lumped disturbance and input saturation, the nominal AFTSMC control command is deduced

$$\boldsymbol{u}_{a_0} = -\mathbb{J}^+(\boldsymbol{\eta})[K_{\mathrm{SMC}} - \dot{\boldsymbol{\ell}}_\eta + \hat{\boldsymbol{J}}_\delta(\boldsymbol{\eta}, \boldsymbol{w})$$
$$+ \lambda_r \boldsymbol{\chi}_r + (\alpha_e \boldsymbol{e}_\eta + \beta_e \boldsymbol{e}_\eta^{m/n} \mathrm{sign}(\boldsymbol{e}_\eta))] \qquad (18)$$

with λ_r belonging to the positive constants. $\hat{\boldsymbol{J}}_\delta(\boldsymbol{\eta}, \boldsymbol{w})$ denotes the vector value of the lumped disturbance which can be estimated from (10). As for the design of the reaching law of SMC K_{SMC}, a conservative operation is to introduce a large gain into the controller to guarantee the system stability, which will cause the gain overestimation. So, a substantial improvement by designing the adaptive mechanism is performed, where the controller gains are adapted to the additive perturbations with unknown boundaries. The reaching law is put forward as follows:

$$K_{\mathrm{SMC}} = K_1 \boldsymbol{S}_r + K_2 |\boldsymbol{S}_r|^p \mathrm{sign}(\boldsymbol{S}_r) \qquad (19)$$

with the adaptive structure as

$$\dot{K}_2(t) = \begin{cases} k_\alpha \mathrm{sign}(|\boldsymbol{S}_r| - \mu), & K_2(t) > K_{\min} \\ K_{\min}, & K_2(t) \le K_{\min} \end{cases} \qquad (20)$$

where $K_1, K_{\min}, k_\alpha \in \mathcal{R}_+$ and $0 < p < 1$. $\mu \in \mathcal{R}_+$ is the threshold detecting loss of the sliding mode. The adaptive mechanism can regulate $K_2(t)$ at the rate k_α to reject the disturbance and ensure the sliding vector converges to the small vicinity of the reference within the finite time [40]. Once the sliding vector reaches the sliding surface, $K_2(t)$ is defined with the constant minimum rate $K_{\min}$. This controller can adapt gains to establish minimal effort and guarantee the system stability while avoiding chattering issue.

The following lemmas are used for the stability analysis of the sliding phase.

Lemma 3 [41]: Suppose $(\alpha, \beta) \in \mathbb{R}$, the following Young's inequality satisfies: $\alpha\beta \le \varepsilon^\rho |\alpha|^\rho /.\rho + |\beta|^q / (\varepsilon^q q).$, once $\varepsilon > 0$, $\rho > 1$, and $q > 1$ meet $(\rho - 1)(q - 1) = 1$.

Lemma 4 [42]: For any real number $\alpha > 0$, $\beta > 0$, and $0 < \rho < 1$, an extended Lyapunov condition of finite-time stability can be given

$$\dot{V}(\mathbf{x}) + \alpha V(\mathbf{x}) + \beta V^\rho(\mathbf{x}) \le 0$$

where the settling time can be estimated by

$$T_f \le t_0 + \frac{1}{\alpha(1 - \rho)} \ln \frac{\alpha V^{1-\rho}(t_0) + \beta}{\beta}.$$

Lemma 5 [42]: Considering the system $\mathbf{R} = f(\mathbf{x}(t))$, an extended Lyapunov condition of practical finite-time stability can be guaranteed with the form as

$$\dot{V}(\mathbf{x}) \le -\alpha V(\mathbf{x}) - \beta V^\rho(\mathbf{x}) + \varepsilon$$

with $\alpha, \beta \in \mathcal{R}_+$, $0 < \rho < 1$, and $0 < \varepsilon < \infty$. Then, the system trajectory $\dot{\mathbf{x}} = \mathbf{x}(t)$ is practical finite-time stable and converges into the bounded region. The residual set of the solution of this system is given by $Q_{\mathrm{region}} = \{\lim_{t \to T_f} \mid V(\mathbf{x}) \le \min\{\varepsilon_0/\alpha, (\varepsilon_0/\beta)^{1/\rho}\}\}$ with $\varepsilon_0 = \varepsilon/(1 - \theta_0)$ and $\theta_0 \in (0, 1)$. The finite settling time is estimated by

$$T_f \le \max \begin{cases} t_0 + \frac{1}{\theta_0 \alpha(1-\rho)} \ln \frac{\theta_0 \alpha V^{1-\rho}(t_0) + \beta}{\beta} \\ t_0 + \frac{1}{\alpha(1-\rho)} \ln \frac{\alpha V^{1-\rho}(t_0) + \theta_0 \beta}{\theta_0 \beta} \end{cases}.$$

C. Stability Analysis

Considering the dynamic model of the helical millirobot in the presence of the lumped disturbance and the input saturation, satisfying the Assumptions 1 and 2, the AFTSMC and the auxiliary system can guarantee that the tracking errors will eventually converge to the small range around the origin in finite time. The compound Lyapunov function candidate is defined as

$$V = \frac{1}{2} S_r^2 + \frac{1}{2} \chi_r^2 + \frac{1}{2} \tilde{K}_2^2 \qquad (21)$$

which is composed of $V_r = (1/2) S_r^2 + (1/2) \chi_r^2$ to verify the global stability and $V_k = (1/2) \tilde{K}_2^2$ to describe the internal convergence of the adaptive gain. $\tilde{K}_2 = \hat{K}_2 - \bar{K}_2$ is the parameter adaption error. Taking the first-order derivative of the Lyapunov function V_r yields

$$\dot{V}_r = S_r \dot{S}_r + \chi_r \dot{\chi}_r. \qquad (22)$$

In consideration of the nominal control law and the auxiliary system, substituting (18) and $u_a = u_{a_0} + \Delta u_a$ into (16), and setting $\Delta u = J(\eta) \Delta u_a$ will lead to

$$\dot{S}_r = -K_1 S_r - \lambda_r \chi_r - \hat{K}_2 S_r^p + \Delta u. \qquad (23)$$

Based on Lemma 3, the inequalities $-\lambda_r \chi_r S_r \le (\lambda_r^2 S_r^2 / 2) + (\chi_r^2 / 2)$, $\rho_r \chi_r \Delta u \le (\rho_r^2 \Delta u^2 / 2) + (\chi_r^2 / 2)$ and $S_r \Delta u \le (S_r^2 / 2) + (\Delta u^2 / 2)$ can be satisfied. In view of (17), (20), and (23), the derivation of the Lyapunov function V_r leads to

$$\dot{V}_r \le -S_r * \left(K_1 S_r + \lambda_r \chi_r + \hat{K}_2 S_r^p \right) + S_r \Delta u$$
$$- k_1 \chi_r^2 - F(\chi_r) \chi_r \frac{|S_r \Delta u| + 0.5 \rho_r^2 \Delta u^2}{\chi_r}$$
$$- k_2 \chi_r \mathrm{sig}^\rho(\chi_r) + \rho_r \chi_r \Delta u$$
$$\le -\left(K_1 - \frac{\lambda_r^2}{2} \right) S_r^2 - (k_1 - 1) \chi_r^2 - K_{\min} \left(S_r^2 \right)^{\frac{(p+1)}{2}}$$

$$-k_2\left(\chi_r^2\right)^{\frac{(\rho+1)}{2}} + \frac{\Delta u^2 \rho_r^2 (1 - F(\chi_r))}{2}$$
$$-|S_r \Delta u|(F(\chi_r) - \text{sign}(S_r \Delta u)). \quad (24)$$

Then, we will prove that the trajectory of tracking errors eventually converge to the small compact set from the two cases.

Case 1: For $F(\chi_r) < 1$, (24) can be rearranged as follows:

$$\dot{V}_r \le -\left(K_1 - \frac{\lambda_r^2}{2}\right)S_r^2 - (k_1 - 1)\chi_r^2 - K_{\min}\left(S_r^2\right)^{\frac{(p+1)}{2}}$$
$$-k_2\left(\chi_r^2\right)^{\frac{(\rho+1)}{2}} + \frac{\Delta u^2 \rho_r^2}{2} + S_r \Delta u$$
$$\le -\kappa_a V_r - \kappa_b V_r^{\frac{(\rho+1)}{2}} + \varepsilon_r$$

where $\kappa_a = \min\{2K_1 - \lambda_r^2 - 1, 2k_1 - 2\}$, $\kappa_b = \min\{2^{([\rho+1]/2)} K_{\min}, 2^{([\rho+1]/2)} k_2\}$, and $\varepsilon_r = [\Delta u^2(\rho_r^2 + 1)/2]$.

With the aid of Lemma 5, the tracking signals are bounded in the small neighborhoods around the origin $Q_{\text{region}} = \{\lim_{t \to T_f} |V(\mathbf{x})| \le \min\{[\varepsilon_r/(1 - \theta_0)k_a], (\varepsilon_r/[(1 - \theta_0)k_b])^{2/(\rho+1)}\}\}$ with $\theta_0 \in (0, 1)$ in finite time T_2

$$T_2 \le \max \left\{ \begin{matrix} T_0 + \frac{2}{\theta_0 k_a(1-\rho)} \ln \frac{\theta_0 k_a V^{\frac{1-\rho}{2}}(t_0) + k_b}{k_b} \\ T_0 + \frac{2}{k_a(1-\rho)} \ln \frac{k_a V^{\frac{1-\rho}{2}}(t_0) + \theta_0 k_b}{\theta_0 k_b} \end{matrix} \right\}. \quad (25)$$

Since, $S_r^2/2 \le V_r$, it follows that the integral sliding mode surface S_r can reach the bounded region in finite time:

$$|S_r| \le \sqrt{2} * \min \left\{ \frac{\varepsilon_r}{(1 - \theta_0)k_a}, \left(\frac{\varepsilon_r}{(1 - \theta_0)k_b}\right)^{2/(\rho+1)} \right\}.$$

Therefore, it means that S_r is bounded in the small set around zero, which subsequently implies that χ_r is uniformly bounded similarly.

Case 2: For $F(\chi_r) = 1$, it implies that $\varepsilon_r = 0$, (24) can be rearranged as follows: $\dot{V}_r \le -(K_1 - [\lambda_r^2/2])S_r^2 - (k_1 - 1)\chi_r^2 - K_{\min}(S_r^2)^{[(p+1)/2]} - k_2(\chi_r^2)^{[(\rho+1)/2]}$. Therefore, $\dot{V}_r + \kappa_a V_r + \kappa_b V_r^{[(\rho+1)/2]} \le 0$ with $\kappa_a = \min\{2K_1 - \lambda_r^2, 2k_1 - 2\}$, $\kappa_b = \min\{2^{([\rho+1]/2)} K_{\min}, 2^{([\rho+1]/2)} k_2\}$. Based on Lemma 4, the settling time can be estimated by:

$$T_2 \le T_0 + \frac{2}{k_a(1 - \rho)} \ln \frac{k_a V^{\frac{1-\rho}{2}}(t_0) + k_b}{k_b}. \quad (26)$$

During the reaching phase from the initial state to the sliding state, it is reasonable to assume that here exists an upper bound $\bar{K}_2$ of the adaptive gain $\hat{K}_2$ until the sliding manifold can be reached ($|S_r| < u$). To analyse the internal convergence of the adaptive gain, deriving the function V_k

$$\dot{V}_k = \tilde{K}_2 \dot{\hat{K}}_2 = \left(\hat{K}_2 - \bar{K}\right) k_\alpha \text{sign}(S_r - u). \quad (27)$$

During the reaching phase, $|S_r| > u$ and $\hat{K}_2 < \bar{K}_2$ are established. So, the condition $\dot{V}_k < 0$ can be satisfied, indicating the existence of a finite time during which the adaptive gain converges. Furthermore, during the sliding phase, $\dot{V}_k = (\hat{K}_2 - \bar{K})K_{\min} < 0$ can also be guaranteed.

To further demonstrate that the tracking errors would drive into small compact sets, we need to consider the Lyapunov function as

$$V_e = \frac{1}{2}e_\eta^2. \quad (28)$$

As the derivative of e_η can be expressed as: $\dot{e}_\eta = \dot{S}_r - \alpha_e e_\eta - \beta_e e_\eta^{m/n} \text{sign}(e_\eta)$, the derivative of V_e will lead to

$$\dot{V}_e = e_\eta\left(\dot{S}_r - \alpha_e e_\eta - \beta_e e_\eta^{m/n} \text{sign}(e_\eta)\right). \quad (29)$$

Since, S_r, χ_r, and K_2 will converge to the small region around origin, (29) can be derived as $\dot{V}_e \le -2\alpha_e V_e - 2^{(m+n)/2n} \beta_e V_e^{(m+n/2n)}$. According to Lemma 4, the tracking error will converge to a bounded region in finite time. Hence, this ends the proof.

Remark 2: Concerning the coefficients selection guideline of the proposed FTDOB, the choice of the parameters $\lambda_{\beta 1}$ and $\lambda_{\beta 2}$ is a tradeoff process. To be specific, a big value for $\lambda_{\beta 1}$ and $\lambda_{\beta 2}$ can correspond to the high-precision estimation and improve the convergence rate, but in turn causes excessive transient peaking in the output response. The fixed gain $K_1 \in \mathcal{R}_+$ in the proposed controller is chosen to satisfy the condition $\kappa_a = \min\{2K_1 - \lambda_r^2 - 1, 2k_1 - 2\} > 0$. Both α_e and β_e are strictly the positive constants, which influence the convergence rate of the tracking error. The parameters k_1 and k_2 denote the positive gain constants in the design of the auxiliary system, which are tuned to satisfy $\kappa_a > 0$ and $\kappa_b > 0$.

IV. EXPERIMENTS AND RESULT

This section demonstrates the performance of the proposed control framework through the physical experiment containing the comparative analysis.

A. Experimental Setup and Procedure

The 3-D printed prototype millirobot (diameter: 1.8 mm and length: 10 mm) contains an NdFeB permanent magnet (diameter: 1 mm and length: 2 mm) inserted at its head, with the dipole moment of the magnet in the direction perpendicular to the central axis. An electromagnetic actuation system (EMA) is constructed to characterize the closed-loop locomotion for the helical millirobot as shown in Fig. 4(a). This platform employs the three laboratory-made electromagnetic coils mounted on the three independently controlled serial manipulators (SJ-603-A and Anno Robot), which can follow the central position of the helical millirobot over a wide area. By superposing three linearly independent magnetic field vectors, three electromagnetic coils can collaboratively generate desired rotating fields in any principal direction at any spatial point within the workspace. Table I summarizes the technical specifications of the mobile electromagnetic system. For real-time visual tracking of the millirobot, two cameras (MER2-160-227U3C and DaHeng) are placed orthogonally in the system, and the YOLO deep learning architecture has been implemented to track the millirobot's position in real time. Moreover, the entire software architecture is constructed using the robot operating system (ROS) to regulate the communication between the electromagnetic system and the proposed control framework.
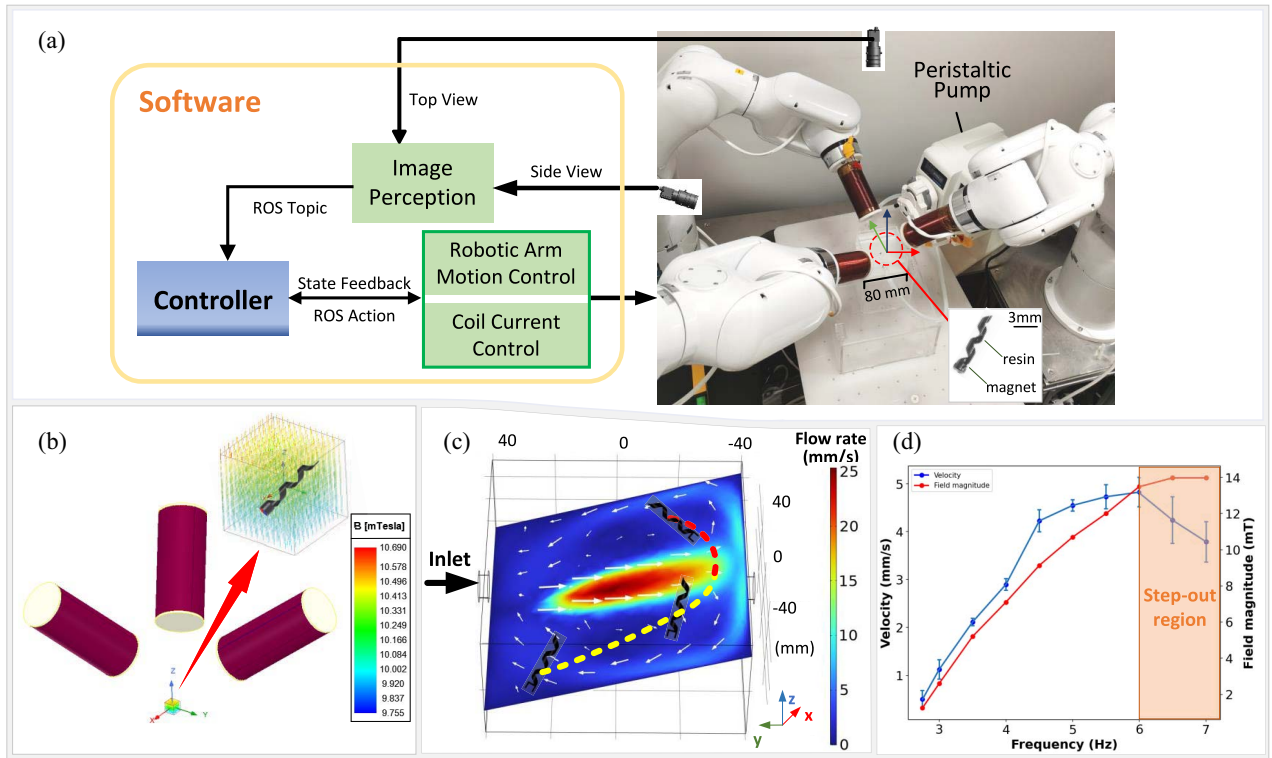
Fig. 4.   Overview framework of the experimental setup. (a) EMA and its closed-loop control framework. The magnetic actuation system can adjust the position of the electromagnetic coils to keep pace with the helical millirobot. In addition, the peristaltic pump is used to generate fluid flow environments. (b) Magnetic field distribution (desired field: [0, 0, 10 mT]) generated by the EMA in a cubic space with a side length of 10 mm, centered at the helical millirobot's position. (c) Flow rate distribution around the given reference path. The yellow and red line represent the upstream and downstream navigation, respectively. (d) Blue line illustrates the frequency dependency of the velocity showing the evolution of the locomotion performance of the helical millirobot, while the red line provides the information about the recommended field magnitude required to achieve the corresponding frequency.

TABLE I
SPECIFICATIONS OF MOBILE ELECTROMAGNETIC SYSTEM

Specifications	Parameter	Value
	Workspace Size (L*W*H)	450*300*350 mm^3
	Communication Interface	ROS
	Mganetic Field	Up to 14 mT
	DOFs	6
	Payload	3 Kg
	Working Radius	540 mm
	Overall Diameter	50 mm
	Coil Length	110 mm
	Wire Diameter	0.9 mm

Given the flexible mobility property of the electromagnetic system, we only need to consider the magnetic field in its region of interest, which is defined as a cubic space with side length of 10 mm centered at the location of the millirobot. To further investigate the local uniformity of the generated magnetic field, the field characteristics of the target region are modeled via ANSYS Electromagnets (ANSYS, Inc., USA). When the desired value of the magnetic field is [0, 0, 10 mT], the spatial distribution of magnetic field in the cubic space is shown in Fig. 4(b), indicates that the uniformity error of the magnetic field is less than 10%. Considering the millimeter-scale size of the helical millirobot and the mobility of the coils, it is realistic to assume that the magnetic field around a millirobot can be modeled uniformly.

The 3-D navigation of the helical millirobot is conducted in an open tank with dimensions of $80 \times 80 \times 40$ mm^3 (length $\times$ width $\times$ height); 85 wt% glycerol fills the tank to facilitate the simulation of the low Reynold number environment, while a tunable peristaltic pump is connected to the tank for generating the fluid flow. It is worth emphasizing that the flow rate is complex in the fluid tank. Fig. 4(c) illustrates the instantaneous distribution of the flow rate on the profile of one reference plane calculated by COMSOL multiphysics when the flow rate at the inlet is 50 mm/s. During tracking the reference path, the helical millirobot will experience the downstream and upstream navigation in two stages. In addition, we have demonstrated that the locomotion performance of the helical millirobot rapidly degrades once it violates the step-out characteristic frequency (6 Hz) as shown in Fig. 4(d). Therefore, the proposed control framework considers the saturation constraint of the rotating field frequency to ensure the tracking performance in a fluid flow environment.

B. Scenario I: Targeted Hovering

In the context of a dynamic biofluid environment, where the goal is to achieve the targeted drug delivery at the desired
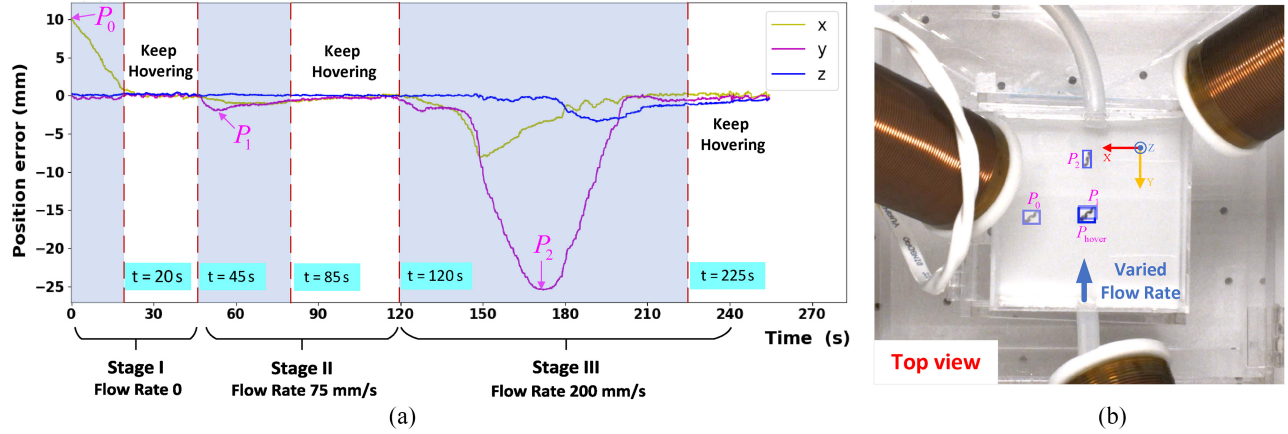
Fig. 5. Results of targeted hovering of the helical millirobot under varied fluid flow. (a) Evolution of position errors of the helical millirobot. The whole process is composed of three stages: 1) Stage I: converging to the targeted hovering position under the flow rate of 0 mm/s; 2) Stage II: applying flow rate of 75 mm/s and the helical millirobot can return to the targeted hovering position under the regulation of the proposed control framework; and 3) Stage III: with a flow rate of 200 mm/s, the helical millirobot returns to the targeted hovering position despite experiencing a significant position deviation. (b) Top-view key snapshots of the experiment process. P_0 denotes the starting position and P_{hover} represents the targeted hovering position. Besides, P_1 and P_2 show the maximum offset positions at the flow rate of 75 and 200 mm/s, respectively.

lesion site using a magnetic robot, our proposed method enables the millirobot to perform precise drug release through targeted hovering. To validate the robustness of the proposed method, three sets of flow rates (0, 75, and 200 mm/s) at the inlet were applied to assess the targeted hovering performance of the helical millirobot.

In Fig. 5(a), it is observed that the helical millirobot's initial position (10 mm, 0, 0) was 10 mm away from the targeted hovering position (0, 0, 0). Here, we define the helical millirobot to enter the hovering state P_{hover} when its relative position remains within the specified error band of ± 1 mm with respect to the targeted hovering position. At the beginning of the experiment when the flow rate was set to 0, the millirobot could converge to the targeted hovering position at $t = 20$ s and maintain the hovering state P_{hover} from $t = 20$ s to $t = 45$ s. When a flow rate of 75 mm/s was introduced at $t = 45$ s, the helical millirobot experienced a maximum displacement of 4.5 mm, being pushed away from the hovering position (Fig. 5(b) and supplementary video S1). By leveraging flow disturbance estimation and control input regulation, the helical millirobot can swim back to the targeted hovering position P_{hover} at $t = 85$ s. Finally, the flow rate was increased to 200 mm/s at $t = 120$ s, resulting in a maximum displacement of 26 mm for the helical millirobot. The proposed method can regulate the rotation frequency and heading of the millirobot, still enable the helical millirobot to withstand the flow disturbance and bring the millirobot back to its hovering state P_{hover} at $t = 225$ s. These experimental results clearly demonstrate the efficacy of the proposed method in enabling the precise control of the helical millirobots for targeted hovering, even under varying flow rates.

C. Scenario II: Comparisons of 3-D Path Tracking Performance Under Different Control Methods

To verify the proposed method in tracking a reference path under fluid flow conditions, we introduced the preset 3-D path

TABLE II
PARAMETERS OF THREE DIFFERENT CONTROLLERS

Controllers	Parameters
Proposed	$K_1 = 0.7, \lambda_{\beta_1} = 0.8, \lambda_{\beta_2} = 0.8, \lambda_r = 0.3,$ $\alpha_e = 0.1, \beta_e = 0.2, k_1 = 1.5, k_2 = 0.6, \rho_r = 0.3$
SMC	$M_1 = 0.7, M_2 = 0.5$
IBVS-PID	$K_p = 0.05, K_d = 0.03, K_i = 0.02$

shown in Fig. 6(a), while the fluid flow at the inlet was set to a constant 50 mm/s. Moreover, the experiments were also conducted with the IBVS-PID [22] and conventional SMC methods [43] for comparison. The parameters of the different control methods are listed in Table II. To quantitatively analyse the tracking performance of the proposed controller, three evaluation indicators were employed: 1) Euclidean norm of the tracking errors (the displacement deviation between the current position and the reference path); 2) standard deviation (SD) of the tracking error; and 3) tracking completion time.

The path tracking results for the three controllers were contrastively exhibited in Fig. 6 (Supplementary Video S2). From Fig. 6(a), it can be seen that all the methods can successfully control the helical millirobot to converge and track the reference path, whereas they showed different motion performances. Under the proposed control framework, the millirobot could track smoothly along the reference path against the fluid flow. In contrast, the tracking path of the SMC and IBVS-PID methods showed significant fluctuations, and the path deviation was more evident than that of the proposed method. From Table III, it could be observed that the proposed method achieved better performance (0.367 ± 0.204 mm), compared with SMC (0.680 ± 0.344 mm) and IBVS-PID (0.937 ± 0.502 mm). This indicated that the proposed method exhibited consistent robustness in resisting the variable disturbance, outperforming both the SMC and
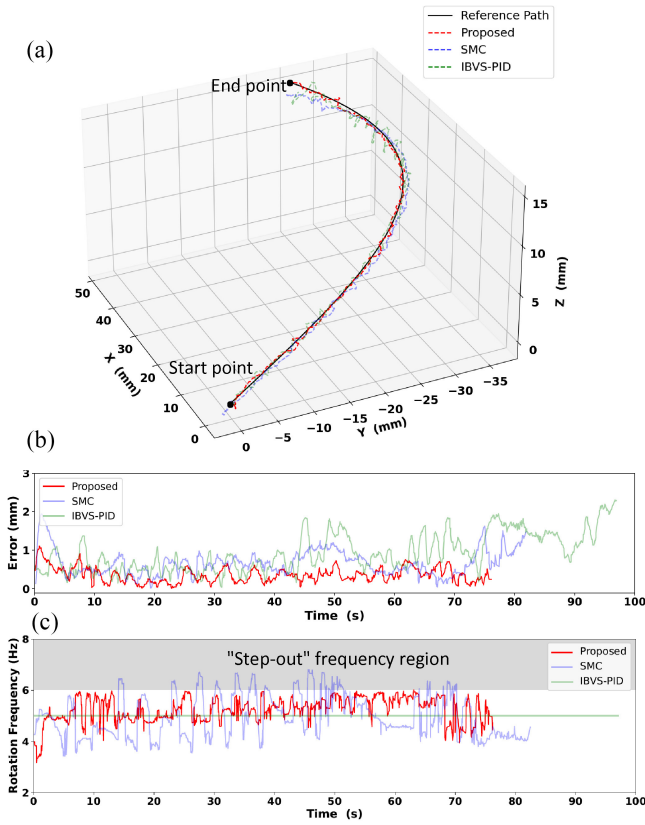
Fig. 6. Comparison results of path following under the proposed control, SMC, and IBVS-PID method. (a) Traces of the helical millirobot's trajectory. (b) Evolution of path following errors. (c) Comparison of the rotating frequency of the magnetic field generated by three different control methods. Note that, the IBVS-PID method maintains a constant rotating frequency of 5 Hz, while the other methods exhibit variations in their rotating frequencies. The gray area denotes the frequency region beyond the step-out characteristic frequency (i.e., 6 Hz in our study).

TABLE III
COMPARISON OF EVALUATION INDICATORS BETWEEN CONTROLLERS

Controllers	Euclidean Norm (mm)	Standard Deviation (mm)	Completion Time (s)
Proposed	**0.367**	**0.204**	**76.2**
SMC	0.680	0.344	82.0
IBVS-PID	0.937	0.502	96.9

IBVS-PID methods. Moreover, our proposed method showed a faster convergence and tracking speed, approximately 76.2 s (SMC: 82.5 s and IBVS-PID: 96.9 s).

As for the anti-saturation ability shown in Fig. 6(c), the rotation frequency of the proposed controller could always be under the predetermined limitation of the step-out characteristic frequency, 6 Hz. In contrast, the SMC violated the limitation of this characteristic frequency, which undermined the control performance. In summary, our method outperformed the SMC and IBVS-PID methods by the designed performance analysis indicators, providing some insights into potential biomedical applications.
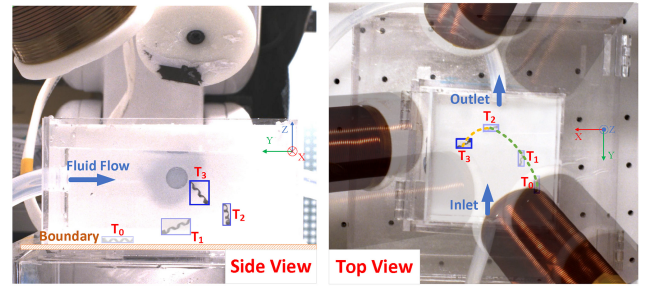

Fig. 7. Top-view and side-view overlaid snapshots of the helical millirobot during the reference path tracking, considering both the boundary effect and the influence of fluid flow.

D. Scenario III: Path Tracking in Different Flow Rate Environments

Now, we consider a more general case, where both the varied fluid flow and the boundary effect are incorporated into the tracking process. Fig. 7 shows the key snapshots of the millirobot in the top view and the side views during the process. The helical millirobot was initially lying and in contact entirely with the substrate surface of the tank. When a helical millirobot started motion, the presence of boundary effect imposed an attractive or repulsive force on the millirobot. During path tracking, the helical millirobot encountered varied flow rates at different stages, and the fluid flow imposed different effects on the millirobot. From T_0 to T_1, the fluid imposed a drag on the robot's movement, while from T_2 to T_3 the fluid flow acted as a push for the robot's movement. It happens to be a scenario that simulates the upstream and downstream tracking processes. The entire process by which the millirobot manages to detach itself from the substrate to overcome the boundary effect, regulate its pose to resist the lumped disturbance, and then converge to the reference path is illustrated in Fig. 7 (supplementary video S3).

Fig. 8 shows the tracking results when the three different sets of flow rates (75, 100, 125 mm/s) were introduced into the system. Despite the varied disturbances, the proposed controller can always successfully navigate the helical millirobot to converge the reference path and maintain around it within minor errors. The first row in Fig. 8 illustrated that the proposed control framework can regulate the rotation frequency and orientation of the helical millirobot in real time to resist the fluid flow and guarantee the tracking performance. When the flow rate switched as a sequence of 75, 100, and 125 mm/s, the tracking completion times were 91.8, 92.8, and 105.4 s, respectively, while the mean errors were 0.445, 0.503, and 0.789 mm, separately. Moreover, the rotation frequency of the helical millirobot in all the cases respected the limitation of the step-out characteristic frequency 6 Hz. This set of experiments can further validate the robustness of the proposed controller without loss of generality.

E. Scenario IV: Actuation of Helical Millirobot in 3-D Tube Dynamic Environments

To investigate the potential capability of our method in targeted drug delivery in the presence of fluid flow, the helical
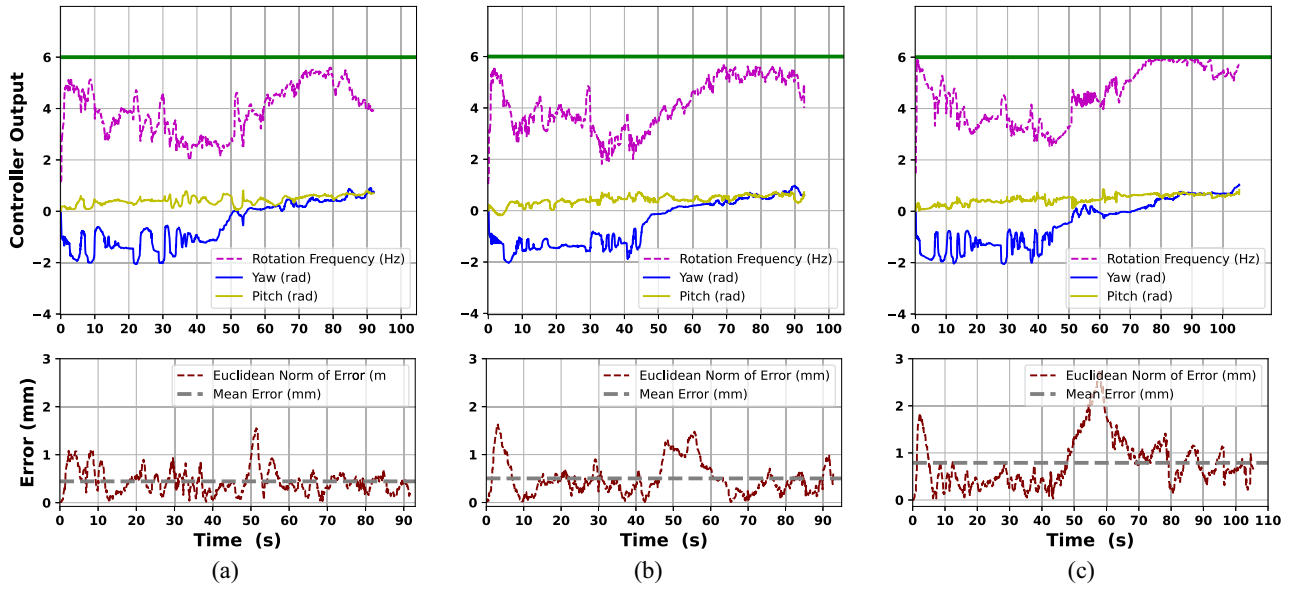
Fig. 8. Results of the 3-D path following under three different flow rates. (a) 75 mm/s. (b) 100 mm/s. (c) 125 mm/s. The first and second row represent the evolution of controller outputs and following errors under three flow rates, respectively.
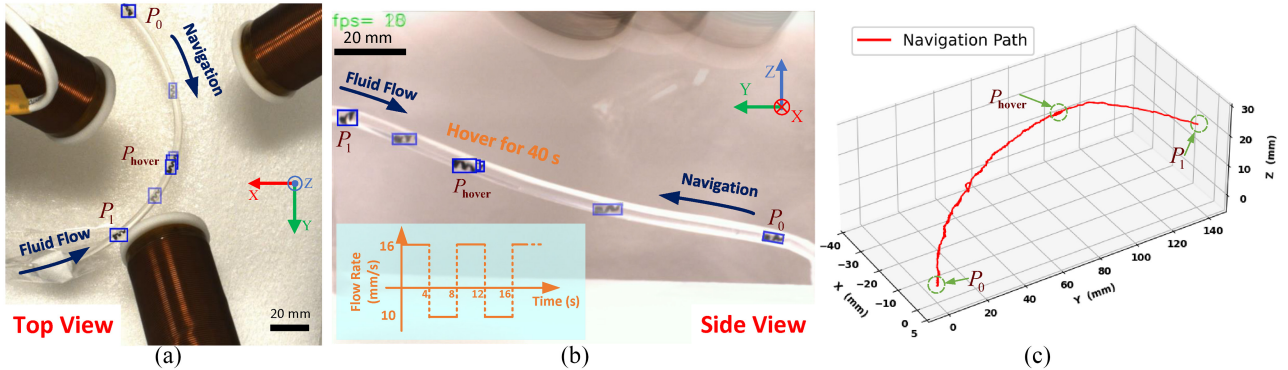

Fig. 9. Top-view (a) and side-view (b) overlaid snapshots of the goal-reaching and hovering process. P_0 denotes the starting position and P_{hover} represents the targeted hovering position. Besides, P_1 shows the navigation endpoint that can be reached within the camera's field of view. (c) Trace of the helical millirobot's trajectory.

millirobot was actuated in a 4-mm-diameter silicon tube, that fills with 80 wt% glycerol for mimicking the drug delivery in a biofluid environment. Note that, the glycerol was flowing through the tube in a pulsatile manner, with a cycle time of 8 s consisting of 4 s of the upstream flow at a rate of 16 mm/s followed by 4 s of the downstream flow at a rate of 10 mm/s. As depicted in Fig. 9(a) and (b) (supplementary video S4), the experimental procedure can be divided into three stages. First, the helical millirobot moved from the starting position P_0 to the hovering position P_{hover}. It then mimicked the drug release process while hovering in P_{hover}. After 40 s of hovering to complete the drug release, the helical millirobot continued to swim forward and completed the remaining path until it reached the endpoint P_1. Fig. 9(c) shows the entire navigation path. The experimental results demonstrate the effectiveness of our method in achieving the hovering task and goal-reaching in pulsatile flowing environments. This study provides valuable insights into the potential capability of our approach for the targeted drug delivery under the influence of biofluid flow.

V. CONCLUSION

In this study, we investigated an AFTSMC with an FTDOB for the 3-D path tracking of a magnetic helical millirobot in complex fluids. The kinematic model of a helical millirobot under the magnetic actuation has been constructed using the 3-D hand position approach. The AFTSMC method integrated with the FTDOB was then designed to determine the guidance law, incorporating an auxiliary dynamics system to solve the input saturation. The stability of the control method was analysed by the Lyapunov functions. Furthermore, utilizing a robotically-actuated magnetic manipulation system, the tracking performance of the proposed control framework was demonstrated through the experimental application to the helical millirobots in complex fluids. In summary, this study qualifies as a first step for the future work on the FTDOB-based adaptive sliding mode control for the helical millirobot actuated by the mobile electromagnetic system. Future research will focus on addressing the challenges associated with interactions with human tissues and biofluid flow

rates *in vivo* when deploying the medical imaging-guided millirobots for minimally invasive therapy.

REFERENCES

[1] P. E. Dupont et al., "A decade retrospective of medical robotics research from 2010 to 2020," *Sci. Robot.*, vol. 6, no. 60, 2021, Art. no. eabi8017.
[2] H. Zhou, C. C. Mayorga-Martinez, S. Pané, L. Zhang, and M. Pumera, "Magnetically driven micro and nanorobots," *Chem. Rev.*, vol. 121, no. 8, pp. 4999–5041, 2021.
[3] Y. Dong et al., "Endoscope-assisted magnetic helical micromachine delivery for biofilm eradication in tympanostomy tube," *Sci. Adv.*, vol. 8, no. 40, 2022, Art. no. eabq8573.
[4] J. Li et al., "Development of a magnetic microrobot for carrying and delivering targeted cells," *Sci. Robot.*, vol. 3, no. 19, 2018, Art. no. eaat8829.
[5] M. Cai et al., "Deep reinforcement learning framework-based flow rate rejection control of soft magnetic miniature robots," *IEEE Trans. Cybern.*, vol. 53, no. 12, pp. 7699–7711, Dec. 2023.
[6] X. Yan et al., "Multifunctional biohybrid magnetite microrobots for imaging-guided therapy," *Sci. Robot.*, vol. 2, no. 12, 2017, Art. no. eaaq1155.
[7] I. C. Yasa, H. Ceylan, U. Bozuyuk, A.-M. Wild, and M. Sitti, "Elucidating the interaction dynamics between microswimmer body and immune system for medical microrobots," *Sci. Robot.*, vol. 5, no. 43, 2020, Art. no. eaaz3867.
[8] Q. Wang, X. Du, D. Jin, and L. Zhang, "Real-time ultrasound doppler tracking and autonomous navigation of a miniature helical robot for accelerating thrombolysis in dynamic blood flow," *ACS Nano*, vol. 16, no. 1, pp. 604–616, 2022.
[9] B. J. Nelson, S. Gervasoni, P. W. Y. Chiu, L. Zhang, and A. Zemmar, "Magnetically actuated medical robots: An in vivo perspective," *Proc. IEEE*, vol. 110, no. 7, pp. 1028–1037, Jul. 2022.
[10] Z. Li et al., "Multifunctional spirulina-hybrid helical microswimmers: Imaging and photothermal efficacy enabled by intracellular gold deposition," *Chem. Eng. J.*, vol. 487, May 2024, Art. no. 150584.
[11] Y. Niu, R. Zhang, and J. Yuan, "Flagellar motors of swimming bacteria contain an incomplete set of stator units to ensure robust motility," *Sci. Adv.*, vol. 9, no. 44, 2023, Art. no. eadi6724.
[12] Y. Dong, L. Wang, V. Iacovacci, X. Wang, L. Zhang, and B. J. Nelson, "Magnetic helical micro-/nanomachines: Recent progress and perspective," *Matter*, vol. 5, no. 1, pp. 77–109, 2022.
[13] T. Xu, G. Hwang, N. Andreff, and S. Régnier, "Planar path following of 3-d steering scaled-up helical microswimmers," *IEEE Trans. Robot.*, vol. 31, no. 1, pp. 117–127, Feb. 2015.
[14] X. Wang et al., "A three-dimensional magnetic tweezer system for intraembryonic navigation and measurement," *IEEE Trans. Robot.*, vol. 34, no. 1, pp. 240–247, Feb. 2018.
[15] L. Yang, M. Sun, M. Zhang, and L. Zhang, "Multimodal motion control of soft ferrofluid robot with environment and task adaptability," *IEEE/ASME Trans. Mechatronics*, vol. 28, no. 6, pp. 3099–3109, Dec. 2023.
[16] Y. Liu, H. Chen, Q. Zou, X. Du, Y. Wang, and J. Yu, "Automatic navigation of microswarms for dynamic obstacle avoidance," *IEEE Trans. Robot.*, vol. 39, no. 4, pp. 2770–2785, Aug. 2023.
[17] M. Medina-Sánchez and O. G. Schmidt, "Medical microbots need better imaging and control," *Nature*, vol. 545, no. 7655, pp. 406–408, 2017.
[18] L. Yang, J. Jiang, X. Gao, Q. Wang, Q. Dou, and L. Zhang, "Autonomous environment-adaptive microrobot swarm navigation enabled by deep learning-based real-time distribution planning," *Nat. Mach. Intell.*, vol. 4, no. 5, pp. 480–493, 2022.
[19] C. Samson, "Control of chained systems application to path following and time-varying point-stabilization of mobile robots," *IEEE Trans. Autom. Control*, vol. 40, no. 1, pp. 64–77, Jan. 1995.
[20] F. Zhao, W. Rong, L. Wang, and L. Sun, "Automatic control of magnetic helical microrobots for on-plane docking," *IEEE Trans. Autom. Sci. Eng.*, early access, Mar. 25, 2024, doi: 10.1109/TASE.2024.3379226.
[21] H. Zhao, J. Leclerc, M. Feucht, O. Bailey, and A. T. Becker, "3D path-following using MRAC on a millimeter-scale spiral-type magnetic robot," *IEEE Robot. Autom. Lett.*, vol. 5, no. 2, pp. 1564–1571, Apr. 2020.
[22] J. Leclerc, H. Zhao, D. Bao, and A. T. Becker, "In vitro design investigation of a rotating helical magnetic swimmer for combined 3-D navigation and blood clot removal," *IEEE Trans. Robot.*, vol. 36, no. 3, pp. 975–982, Jun. 2020.
[23] X. Wu, J. Liu, C. Huang, M. Su, and T. Xu, "3-D path following of helical microswimmers with an adaptive orientation compensation model," *IEEE Trans. Autom. Sci. Eng.*, vol. 17, no. 2, pp. 823–832, Apr. 2020.
[24] L. Yang, Z. Yang, M. Zhang, J. Jiang, H. Yang, and L. Zhang, "Optimal parameter design and microrobotic navigation control of parallel-mobile-coil systems," *IEEE Trans. Autom. Sci. Eng.*, vol. 21, no. 1, pp. 855–867, Jan. 2024.
[25] Z. Zhu, Y. Xia, and M. Fu, "Attitude stabilization of rigid spacecraft with finite-time convergence," *Int. J. Robust Nonlin. Control*, vol. 21, no. 6, pp. 686–702, 2011.
[26] B. J. Nelson, I. K. Kaliakatsos, and J. J. Abbott, "Microrobots for minimally invasive medicine," *Annu. Rev. Biomed. Eng.*, vol. 12, pp. 55–85, Aug. 2010.
[27] W. He, Z. Yan, C. Sun, and Y. Chen, "Adaptive neural network control of a flapping wing micro aerial vehicle with disturbance observer," *IEEE Trans. Cybern.*, vol. 47, no. 10, pp. 3452–3465, Oct. 2017.
[28] Z. Yang, L. Yang, and L. Zhang, "Autonomous navigation of magnetic microrobots in a large workspace using mobile-coil system," *IEEE/ASME Trans. Mechatronics*, vol. 26, no. 6, pp. 3163–3174, Dec. 2021.
[29] Y. Chen, J. Liang, Y. Wu, Z. Miao, H. Zhang, and Y. Wang, "Adaptive sliding-mode disturbance observer-based finite-time control for unmanned aerial manipulator with prescribed performance," *IEEE Trans. Cybern.*, vol. 53, no. 5, pp. 3263–3276, May 2023.
[30] A. Mohammadi and M. W. Spong, "Integral line-of-sight path following control of magnetic helical microswimmers subject to step-out frequencies," *Automatica*, vol. 128, Jun. 2021, Art. no. 109554.
[31] A. W. Mahoney, J. C. Sarrazin, E. Bamberg, and J. J. Abbott, "Velocity control with gravity compensation for magnetic helical microswimmers," *Adv. Robot.*, vol. 25, no. 8, pp. 1007–1028, 2011.
[32] L. Consolini and M. Tosques, "A minimum phase output in the exact tracking problem for the nonminimum phase underactuated surface ship," *IEEE Trans. Autom. Control*, vol. 57, no. 12, pp. 3174–3180, Dec. 2012.
[33] J. O. A. L. Filho, E. L. F. Fortaleza, and M. C. M. M. de Campos, "A derivative-free nonlinear Kalman filtering approach using flat inputs," *Int. J. Control*, vol. 95, no. 11, pp. 2900–2910, 2022.
[34] K. D. Do, Z. P. Jiang, and J. Pan, "Robust adaptive path following of underactuated ships," *Automatica*, vol. 40, no. 6, pp. 929–944, 2004.
[35] A. Levant, "Higher-order sliding modes, differentiation and output-feedback control," *Int. J. Control*, vol. 76, nos. 9–10, pp. 924–941, 2003.
[36] J. A. Moreno and M. Osorio, "Strict Lyapunov functions for the super-twisting algorithm," *IEEE Trans. Autom. Control*, vol. 57, no. 4, pp. 1035–1040, Apr. 2012.
[37] G. Peng, C. Yang, W. He, and C. L. P. Chen, "Force sensorless admittance control with neural learning for robots with actuator saturation," *IEEE Trans. Ind. Electron.*, vol. 67, no. 4, pp. 3138–3148, Apr. 2020.
[38] Y. Yu, C. Guo, and T. Li, "Finite-time LOS path following of unmanned surface vessels with time-varying sideslip angles and input saturation," *IEEE/ASME Trans. Mechatronics*, vol. 27, no. 1, pp. 463–474, Feb. 2022.
[39] Z. Zheng and M. Feroskhan, "Path following of a surface vessel with prescribed performance in the presence of input saturation and external disturbances," *IEEE/ASME Trans. Mechatronics*, vol. 22, no. 6, pp. 2564–2575, Dec. 2017.
[40] H. Castañeda, J. Rodriguez, and J. L. Gordillo, "Continuous and smooth differentiator based on adaptive sliding mode control for a quad-rotor MAV," *Asian J. Control*, vol. 23, no. 2, pp. 661–672, 2021.
[41] G. H. Hardy, J. E. Littlewood, and G. Pólya, *Inequalities*. Cambridge, U.K.: Cambridge Univ. Press, 1952.
[42] J. Yu, P. Shi, and L. Zhao, "Finite-time command filtered backstepping control for a class of nonlinear systems," *Automatica*, vol. 92, pp. 173–180, Jun. 2018.
[43] Y. Shtessel, C. Edwards, L. Fridman, and A. Levant, *Sliding Mode Control and Observation*, New York, NY, USA: Springer, pp. 251–290, 2014.

Zhaoyang Qi (Student Member, IEEE) received the bachelor's degree from Hefei University of Technology, Hefei, China, in 2018, and the master's degree in instrument science and technology from the University of Science and Technology of China, Hefei, China, in 2021. He is currently pursuing the Ph.D. degree with the Department of Mechanical and Automation Engineering, The Chinese University of Hong Kong, Hong Kong, China.

His research interests include intelligent control of medical robotics.

Xurui Liu received the bachelor's degree in opto-electronic information science and engineering from Harbin Institute of Technology, Weihai, China, in 2018, and the master's degree in microelectronics and solid state electronics from Huazhong University of Science and Technology, Wuhan, China, in 2022. He is currently pursuing the Ph.D. degree with the Department of Mechanical and Automation Engineering, Chinese University of Hong Kong, Hong Kong, China.

His research interests include magnetic medical devices and systems.

Mingxue Cai (Member, IEEE) received the Ph.D. degree in control theory and control engineering from the Institute of Automation, Chinese Academy of Sciences, Beijing, China, in 2020.

He was a Postdoctoral Fellow with the Chinese University of Hong Kong, Hong Kong, China, from 2021 to 2023. He is currently working with the Guangdong Provincial Key Laboratory of Robotics and Intelligent System, Shenzhen Institute of Advanced Technology, Chinese Academy of Sciences, Shenzhen, China. His research interests include robotics, intelligent control, and deep reinforcement learning.

Kai Fung Chan received the B.Eng. and Ph.D. degrees in biomedical engineering from the Chinese University of Hong Kong (CUHK), Hong Kong, China, in 2015 and 2019, respectively.

He is currently a Research Assistant Professor with the Chow Yuk Ho Technology Centre for Innovative Medicine, Faculty of Medicine, CUHK. His research interests are: micro-/nanorobotics for minimally invasive endoluminal intervention; micro-robotic sensing platforms for automated pathogen sensing; miniature medical devices for the in vivo diagnosis and treatment of gastrointestinal diseases; and the corresponding translational research.

Bo Hao received the B.S. degree in aircraft design and engineering from Nanjing University of Aeronautics and Astronautics, Nanjing, China, in 2016, the M.S. degree in mechanical and aeronautical engineering from the École Nationale Supérieure de Mécanique et d'Aérotechnique, Poitiers, France, in 2019, and the M.E. degree in mechanical engineering from Nanjing University of Aeronautics and Astronautics, in 2020. He is currently pursuing the Ph.D. degree with the Chinese University of Hong Kong, Hong Kong, China.

His research interest includes small-scale robotics.

Chenguang Yang (Fellow, IEEE) received the B.Eng. degree in measurement and control from Northwestern Polytechnical University, Xi'an, China, in 2005, and the Ph.D. degree in control engineering from the National University of Singapore, Singapore, in 2010.

He was a Postdoctoral Fellow of Human Robotics with the Imperial College London, London, U.K., from 2009 to 2010. He is currently the Chair of Robotics with the Department of Computer Science, University of Liverpool, Liverpool, U.K. His research interest lies in human–robot interaction and intelligent system design.

Dr. Yang was awarded the U.K. EPSRC UKRI Innovation Fellowship and individual EU Marie Curie International Incoming Fellowship. As the lead author, he won the IEEE Transactions on Robotics Best Paper Award in 2012 and the IEEE Transactions on Neural Networks and Learning Systems Outstanding Paper Award in 2022. He is the Corresponding Co-Chair of IEEE Technical Committee on Collaborative Automation for Flexible Manufacturing.

Yanfei Cao received the B.E.degree in mechanical engineering and automation and the M.E. degree in mechanical and electronic engineering from Nanjing University of Aeronautics and Astronautics, Nanjing, China, in 2016 and 2019, respectively. He is currently pursuing the Ph.D. degree with the Department of Mechanical and Automation Engineering, Chinese University of Hong Kong, Hong Kong, China.

His research interests include magnetic actuation, soft materials, and machine learning for medical robots.

Lin Su received the master's degree in instrumentation science and technology from Beihang University, Beijing, China, in 2020, and the Ph.D. degree from the University of Hong Kong, Hong Kong, China, in 2024.

Her research interests include 3-D-printing microbotics for biomedical applications.

Li Zhang (Fellow, IEEE) received the Ph.D. degree from the University of Basel, Basel, Switzerland, in 2007.

He is currently a Professor with the Department of Mechanical and Automation Engineering and a Professor (by courtesy) with the Department of Surgery, Chinese University of Hong Kong, Hong Kong, China. His research interests include microrobotics and nanorobotics for biomedical applications and their collective behaviors for the development of intelligent robot swarms at small scales.